Automated tree ring detection of common Indiana hardwood species through deep learning: Introducing a new dataset of annotated images

Fanyou Wu [a], Yunmei Huang [a], Bedrich Benes [b], Charles C. Warner [a], Rado Gazo [a,*]

[a] Department of Forestry and Natural Resources, Purdue University, West Lafayette, 47906, IN, USA
[b] Department of Computer Science, Purdue University, West Lafayette, 47906, IN, USA

ARTICLE INFO

ABSTRACT

Tree-ring dating enables gathering necessary knowledge about trees, and it is essential in many areas, including forest management and the timber industry. Tree-ring dating can be conducted on either wood's clean cross-sections or tree trunks' rough end cross-sections. However, the measurement process is still time-consuming and frequently requires experts who use special devices, such as stereoscopes. Modern approaches based on image processing using deep learning have been successfully applied in many areas, and they can succeed in recognizing tree rings. While supervised deep learning-based methods often produce excellent results, they also depend on extensive datasets of tediously annotated data. To our knowledge, there are only a few publicly available ring image datasets with annotations. We introduce a new carefully captured dataset of images of hardwood species automatically annotated for tree ring detection. We capture each wood cookie twice, once in the rough form, similar to industrial settings, and then after careful cleaning, that reveals all growth rings. We carefully overlap the images and use them for an automatic ring annotation in the rough data. We then use the Feature Pyramid Network with Resnet encoder that obtains an overall pixel-level area under the curve score of 85.72% and ring level F_1 score of 0.7348. The data and code are available at https://github.com/wufanyou/growth-ring-detection.

1. Introduction

Dendrochronology, also known as tree-ring dating, has been used in a variety of scientific fields, including archaeology, climatology, hydrology, and quaternary geology [1–5]. Besides its scientific applications, tree-ring dating is also useful for forest management and the wood industry. By examining the mean annual ring width of logs, managers can determine the average growth rate of a forest and the wood quality, which can inform their forest management strategies. However, accurately identifying and counting tree rings can be challenging due to variations in ring patterns across species and tree ages. [6] noted that tree-ring measurements can be taken from clean cross-sections of wood or rough end faces of tree trunks, depending on the specific requirements and circumstances of the analysis.

Tree-ring dating often utilizes wood, which is the secondary xylem of tree plants. A single growth ring may contain both earlywood and latewood. Earlywood has thinner cell walls and larger lumens than latewood, and it typically grows at the beginning of the season. In terms of anatomy, softwood (from conifers) and hardwood (from deciduous trees) have different structures. Softwood is simpler, consisting mainly of tracheid cells (90%–95% by mass). In a cross-section, the growth rings of softwood can be distinct or indistinct depending on the transition between earlywood and latewood, the growth rate of the tree, and other factors. Hardwood is more complex and has a greater variety of cell types. Within a single growth cycle, the distribution of pores (cross-sections of vessel elements) varies. Hardwoods can be divided into three categories based on pore distribution: ring-porous (larger pore diameters in earlywood), diffuse-porous (similar pore diameters within one growth ring), and semi-ring-porous (between the two distinct types). The difficulty of accurately detecting growth ring edges in hardwoods is correlated with pore distribution (it is easier in ring-porous species), pore diameter (simpler in species with large pore diameters), and other factors such as wood color. Despite the diversity of hardwood species in cross-section, it remains a challenge to identify ring edges for many hardwood species automatically [7].

Currently, the process of tree-ring measurement is still labor-intensive and often requires the expertise of trained professionals using tools like stereoscopes and software such as WinDENDRO™ or open-source equivalents like MtreeRing [8], which can analyze tree rings from scanned or photographed images. However, the performances of those methods depend on the clarity of the input images. X-ray

(a) Rough surface.
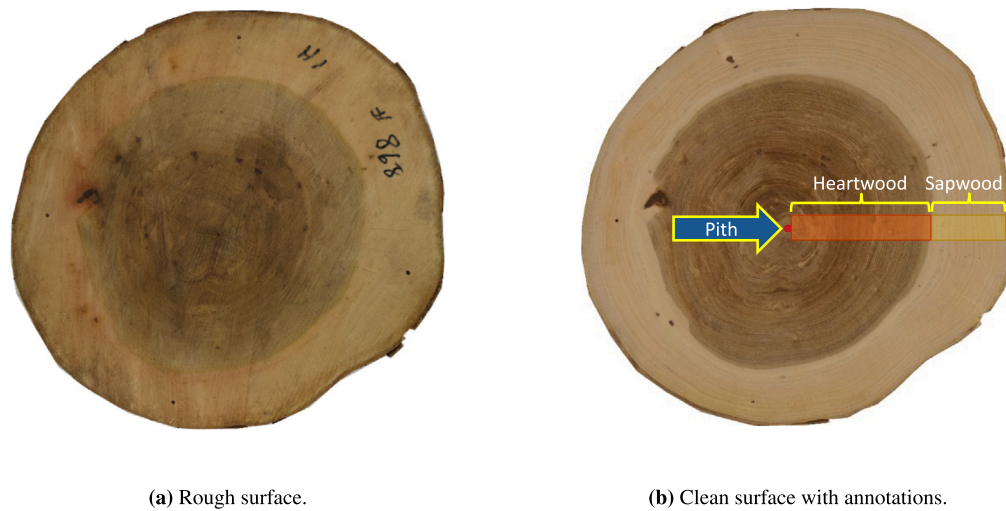
(b) Clean surface with annotations.

Fig. 1. Sample image pair of Hickory (*Carya spp.*). (a) is the rought image and (b) is carefully processed. Both images are then overlap to help training of our deep model to detect growth rings.

a) Raw cookie   b) Aligned   c) Cleaned   d) Annotated   e) Back-mapped Annotations

Fig. 2. Overall process pipeline. The raw cookie (a) is marked with drilled holes (shown schematically as circles) for alignment (b) and then cleaned (c). Two images (one from each side) are then taken and the images are manually annotated (d). The annotations are mapped back to the raw cookie and used to train our deep neural network model.

screening is sometimes used to produce higher quality images that can more easily distinguish ring edges, and some software, like LignoVision™, now supports the use of X-ray images. Surface cleaning or X-ray screening may not be practical or cost-effective in a forest or sawmill setting, so it is still important to find better methods for measuring annual tree ring widths when the surface of the wood logs is rough (Fig. 1(a)).

Image processing methods have been developed to detect and measure tree ring widths automatically. [9] used morphological operations such as erosion and dilation, opening and closing, and watershed segmentation to measure the tree ring area for Norway Spruce semi-automatically (Picea abies L.). [10] employed a Generalized Hough Transform to estimate tree rings with the help of image gradient and edge detection. These types of image processing algorithms are frequently used in tree ring measurement research [11]. However, these methods rely heavily on the assumption that tree ring images from trunks have high-contrast edges and that tree rings have a common circular shape, and they can be prone to failure on images with noise or other patterns.

Deep learning-based methods have also been employed to detect tree rings. [12] treated tree ring detection as a semantic segmentation with U-Net [13]. Similarly, [14] applied pix2pix [15], a derivative from generative adversarial network (GAN) [16], to obtain output ring edges. These supervised learning-based methods often show better results than image processing methods. However, they require larger datasets of annotated images. To our knowledge, there are only a few publicly available ring image datasets with annotations, e.g., in [17], which somehow handle the development of creative machine learning applications for tree ring edge detection.

Our paper makes two key contributions: firstly, the development of a new dataset consisting of annotated images of common hardwood species found in Indiana, aimed at facilitating tree ring detection; and

Table 1
Summary of wood samples.

Species	Common name	Number of cookies
Acer saccharinum	Soft maple	12
Acer saccharum	Hard maple	14
Carya spp.	Hickory	12
Celtis occidentalis	Hackberry	10
Fraxinus spp.	Ash	11
Juglans nigra	Black walnut	14
Liriodendron tulipifera	Yellow poplar	11
Prunus serotina	Cherry	13
Quercus rubra	Red oak	14
Quercus spp.	White oak	14
Tilia americana	Basswood	11
Total		**136**

secondly, the proposal of a deep learning-based method to effectively detect the edges of tree growth rings.

2. Material and methods

2.1. Data collection and processing

We gathered and processed 136 wood cookies (trunk cross sections approximately 10–12 cm thick and 25–60 cm radius) of 11 common Indiana hardwood species (see Table 1 for details).

Fig. 2 shows the overall methodology of the research. The raw cookie (a) has four holes drilled for alignment (indicated by yellow circles in (b)). The cookie is taken to the imagining frame, and two images are taken from both sides. Because it is difficult to see the growth rings in the raw images, we clean the surface of the cookie
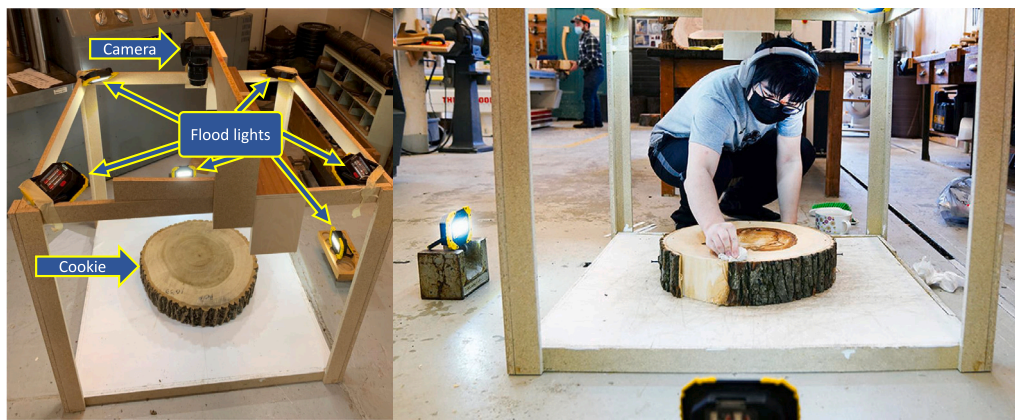
Fig. 3. We built a special imagining frame with fixed light conditions and calibrated camera (marked in the left figure). The camera is situated above the cookie and several flood lights illuminate the surface to ensure pronounced details in the final image. Human for scale (right).

Fig. 4. Annotation Sample of White Oak (*Quercus spp.*).

to increase the visibility of the growth rings (c). The cookie is then transferred again to the imagining frame, and two additional images are taken, one from each side. The growth rings are more visible, and the images are then manually annotated with growth rings (d). Because we know the exact position of the cookie from the alignment step, we can now map the growth rings back to the raw images (e). Below we describe the steps in detail.

2.1.1. Imagining frame

We build a special imagining frame to gather the image data (Fig. 3). The area of the frame is 95×95 cm horizontally, and the camera was situated on the top at a distance of 92 cm. We added six fill lights: four pointing downwards and two parallel to the cross-sections to reduce reflected light spots and self-shadowing. The camera is Nikon Digital Camera D3300, and the lens is: Nikon DX AF-S Nikkor 18-55 mm. We used autofocus (AF) and auto white balance (AWB) to obtain better quality images during the image-taking process, so the pixel area and contrast vary slightly for each wood cookie. An image of each side of the cookie was taken.

2.1.2. Sample preparation

Alignment: We need to align the images before and after the cleaning. To make sure the images have certain shared markers, we drilled four holes on each rough wood surface (surface cut with a chainsaw) as indicated by yellow circles in Fig. 2(b).

Cleaning: After initial rough-surface images were taken, each cookie surface was machined flat using a Model 40 Thermwood Computer numerical control (CNC) router and a fly-cut tool until both sides were flat. The cookies were limited to 19.4 cm in initial height due to the clearance on the router carriage. Depending on the initial cookie roughness, processing any individual side of one cookie could take anywhere from 5 to 25 min. The maximum material that could be taken off in one pass from the router was 0.51 cm. This process was repeated until one side of the cookie was completely flat. Once flat, the cookies were turned over to surfacing the other side. The steps were repeated

until the entire cookie was flat on both sides. By the time the CNC processing was finished, the cookies were flat on both sides but left with small machining marks that would be sanded off in the final step.

The hardwood cookies flat on both sides were sanded with a 60-grit sanding belt using a TimeSaver Series 1300 wide belt sander. Using the TimeSaver belt sander, the cookies were sanded until the machine marks from the fly-cut router bit were eliminated. Like the Thermwood router, the TimeSaver had a height requirement, and no cookies could be bigger than 12.7 cm tall. So before even being considered to sand, the CNC operator machined the cookies down to less than 12.7 cm in height. With each pass through the TimeSaver using 60 grit sandpaper, the maximum amount of material the operator could take off was -0.051 cm. Once finished sanding on both sides, a brush, compressed air, and shop vacuum were used to remove dust from the surface as necessary to achieve clear cross sections for the clean-surface pictures.

The clean-surface picture taking was similar to the rough-surface picture taking process, with the addition that for several species, both dry and wet surface pictures were taken. For many species, wetting the surface with water could remove dust and make the surface features more visible. However, for Black Walnut, the absorbed water will lead to a darker surface and more invisible ring edges.

2.1.3. Data annotation

Data Annotation was performed in two steps. We first manually labeled four markers from the alignment step (East, West, North and South) and the pith coordinates to align the images of both rough and clean images. Then we focused on the clean images. We divide each cookie into four slices starting in the pith of the cookie to the edge of the image, and manually annotated the ring edges (Fig. 2d).

An example of the annotation is in Fig. 4. We annotated the ring edges with clean boundary to avoid potential false positive samples created by human considering that the ring edges are arrange tightly. The annotation was done by marking two or three points and storing the geometric information as a line segment of an arc segment. This was the most time consuming task and it typically took about five minutes
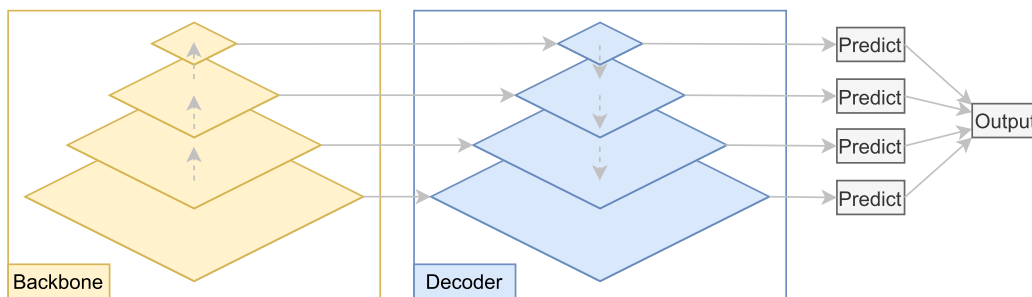
Fig. 5. Illustration of the FPN architecture.

Table 2
Model architecture summary for FPN. The residual block is composed of two convolutional layers.

Component	Input	Output	Layer
Encoder (ResNet-18)	$1 \times 128 \times 128$	$64 \times 64 \times 64$	7×7, stride 2
	$64 \times 64 \times 64$	$64 \times 32 \times 32$	3×3 max pool, stride 2
	$64 \times 32 \times 32$	$e_1^{64 \times 32 \times 32}$	(3×3, 64 residual block)×2
	e_1	$e_2^{128 \times 16 \times 16}$	(3×3, 128 residual block)×2
	e_2	$e_3^{256 \times 8 \times 8}$	(3×3, 256 residual block)×2
	e_3	$e_4^{512 \times 4 \times 4}$	(3×3, 512 residual block)×2
Decoder	e_4	$p_4^{256 \times 4 \times 4}$	(1×1, 256 conv)
	e_4, e_3	$p_3^{256 \times 8 \times 8}$	(1×1, 256 conv)
	e_3, e_2	$p_2^{256 \times 16 \times 16}$	(1×1, 256 conv)
	e_2, e_1	$p_1^{256 \times 32 \times 32}$	(1×1, 256 conv)
	p_1, p_2, p_3, p_4	$1 \times 32 \times 32$	(3×3, 1 conv)

to fully label one slice of each wood cookie. In total, we annotated 19,898 growth rings for those images, and the average number of annotated growth rings for each species is from 23 (Soft maple) to 56 (Ash).

Back-Mapping of the annotations was performed by aligning the rough images with the annotations from the clean ones, by using the physically created markers shown in Fig. 2(d).

2.2. Growth ring detection

This paper uses a two-step method to find the growth ring edges. First, we applied semantic segmentation to find the given image's coarse likelihood map. Then, we use morphology operations to finalize the growth ring edges.

Semantic segmentation: We applied Feature Pyramid Networks (FPN) [18] as image segmentation architecture with the encoder of ResNet-18 [19] (see Fig. 5 for the FPN architecture and Table 2 for details about the structure). We also tested MobileNet [20] and Efficient [21] as the encoders, and we discuss details about the selection of different components in this step and their effects in Section 3.3.

We applied soft Jaccard loss [22,23]:

$$J(y, \hat{y}) = 1 - \frac{(y \cdot \hat{y}) + \varepsilon}{(y + \hat{y} - y \cdot \hat{y}) + \varepsilon}, \qquad (1)$$

where y and $\hat{y}$ are ground truth and prediction respectively, and ε prevents zero division (typically equals to 1^{-7}). Jaccard loss, also known as region-based loss, differs slightly from cross-entropy (a distribution-based loss). These losses minimize the mismatch or maximize the overlap between prediction and ground truth. Jaccard loss is applied here as its objective is close to one evaluation metric in Section 2.3.

To train our model, we used the following hyperparameters: the image size was 128×128 pixels, the batch size was 32 images, the maximum training epochs is 3000 epochs, the optimizer was ADAM [24] and the learning rate was 1×10^{-4}. These parameters were determined through experimentation with various values.

Growth ring extraction from segmentation map: The previous step produces a rough map of the likelihood of the growth rings. To extract the growth rings, we employed a post-processing strategy based on the method described by [12]. Since there is strong evidence that growth rings are successive, it is logical to use local adaptive thresholding. We used the mean-based thresholding and local adaptive contrast method [25] to finalize the growth ring edges. The binary outputs were then skeletonized using the iterative thinning method [26]. Fig. 6 shows an example of the output after these morphological operations.

2.3. Evaluation

We utilized the Area Under the Receiver Operating Characteristic Curve (ROC–AUC) score, or simply AUC, to assess the performance of segmentation models. Other standard metrics, such as accuracy and recall, are not well suited to measuring segmentation performance as they require a pre-defined threshold (typically 0.5 if the dataset is balanced) to do the binarization. However, we trained only one model for the whole species, and it is necessary to calibrate the threshold species individually to achieve the best performance. Also, because our proposed method includes post-processing, we are more concerned with the prediction's local maximum than its absolute value.

To evaluate the accuracy of growth ring detection, we define detected tree-ring boundaries rightly as true positives (TP), tree-ring boundaries missed by models as false negatives (FN), and false boundaries identified by models as false positives (FP). Specifically, a TP is defined as an area with an overlap of more than 25% of the width; anything else is considered an FN. The 25% threshold is mainly determined by the task's difficulty. An FP is determined if the overlap between two successive growth ring edges is more than 25% of the width. We use these values to define the recall (REC):

$$REC = \frac{TP}{TP + FN}, \qquad (2)$$

and precision (PREC) is :

$$PREC = \frac{TP}{TP + FP}. \qquad (3)$$

Raw Image

Likelihood Map

Threshold Map

Skeletonized Map

Ground Truth

Fig. 6. Sample results.

Table 3
The performance over different species on clean surface.

Species	Common name	AUC	PREC	REC	F_1
Acer saccharinum	Soft maple	84.09%	0.5435	0.8534	0.6621
Acer saccharum	Hard maple	85.81%	0.6143	0.8743	0.7176
Carya spp.	Hickory	86.70%	0.6744	0.8828	0.7614
Celtis occidentalis	Hackberry	82.80%	0.6998	0.8684	0.7714
Fraxinus spp.	Ash	88.52%	0.8052	0.8878	0.8402
Juglans nigra	Black walnut	84.05%	0.5921	0.7067	0.6341
Liriodendron tulipifera	Yellow poplar	85.13%	0.5694	0.9012	0.6958
Prunus serotina	Cherry	85.92%	0.7011	0.7831	0.7338
Quercus rubra	Red oak	88.14%	0.6497	0.9163	0.7563
Quercus spp.	White oak	87.19%	0.6838	0.9097	0.7749
Tilia americana	Basswood	84.21%	0.7181	0.7964	0.7465

Finally, we use the F_1 score to evaluate the performance, which is the harmonic mean of precision and recall

$$F_1 = 2 \cdot \frac{REC \cdot PREC}{REC + PREC}, \tag{4}$$

3. Results and discussion

We implemented our framework in PyTorch 1.7. All experiments were run on a desktop computer with NVIDIA GeForce RTX 1080 Ti GPU. We used a five-fold data splitting without overlapping, so we trained five models for each setup. The data and code are available here.[1] Below we discuss factors that affected the performance of our methods.

3.1. Species and comparison to related work

Table 3 displays the performance for several species. Overall, the AUC values for all species varied from $AUC \in \langle 0.8 - 0.9 \rangle$, indicating that the segmentation model could rate the probability of the pixel inside a single picture. Not all species perform equally when we evaluate performance under the growth ring level. In particular, black walnut ($F_1 = 0.6341$) and soft maple ($F_1 = 0.6621$) had the lowest F_1 scores. This is in agreement with our intuition and expectation since during the annotating step these two specie samples were the two most difficult species to manually determine the growth ring edges. Our performance is a bit worse than that reported by [12] where the average F_1 score is about 0.96, because we studied more difficult species: hardwood species are anatomically complicated in the cross-section and much harder to detect the growth rings that softwood species. Furthermore, the average distance between two growth rings has a significant impact on performance. The average distance between two successive growth

rings in [12] is roughly 5-10× larger in pixel value than ours, suggesting that certain morphological processes may have failed in our dataset. The failure of morphological processes could also be concluded from the relatively weak correlation of AUC (pixel level) and F_1 (growth ring level).

Table 4
The impacts of surface cleanliness.

Surface	AUC	F_1
Clean Wet	85.72%	0.7348
Clean Dry	79.41%	0.6096
Rough	75.46%	0.5123

3.2. Surface

Another goal of our study was to examine the effect of surface smoothness on ring detection performance. Table 4 shows the impact of surface smoothness. It agrees with our assumption that ring edges from the rough surface are the hardest to identify. Also, wetting the surface makes ring edges more clearly visible both by human eyes and by automatic detection.

3.3. Ablation study

We performed an ablation study to identify the best combination of the process parameters in Table 5. Our proposed method is the best from the perspective of semantic segmentation models. We observed the weak correlation between the pixel AUC and the ring F_1 mainly because the growth ring extraction from the likelihood map is fixed with no parameter fine-tuning.

We used an identical setup to compare the impact of utilizing RGB, HSV, and V (relative lightness or darkness of a color) color space.

---

[1] https://github.com/wufanyou/growth-ring-detection.

Table 5
Ablation Study. The last row is our proposed method.

Component	Setting	AUC	F_1
Loss	Cross Entropy	85.70%	0.5884
Encoder	MobileNet-V2	84.35%	0.5479
	Efficient-b0	85.28%	0.7170
Color Space	HSV	84.40%	0.6924
	RGB	85.96%	0.7336
Proposed		85.72%	0.7348

Utilizing only raw RGB color performs equally well as using the V channel. We conjugate that our hardwood dataset is more complicated, making it harder to rely on the robust prior knowledge that ring edges are often shown when the relative lightness changes abruptly. Also, considering that all the pre-trained models are trained using RGB channel images, it might be helpful to affect the performance of using RGB channels. However, given the subtle difference between RGB and V color channels, we still recommend using a V color channel.

3.4. Limitations

Although it was tedious to gather, the labeled dataset size is relatively small. This dataset size will hurt reproducibility if the random seed is not fixed. For annotation, we utilized four rectangular areas per sample. In certain species, e.g., Black walnut and Soft maple, the growth ring edges were difficult to identify even by trained human eyes. In the future, we should annotate ring edges in more cross-sectional samples and perhaps even the entire cross-section surface.

Additionally, we manually labeled the pith in this research and sliced several images from the pith to the bark edges. In real-world production, the correct localization of the pith is also essential [14,27]. Tree, as a natural plant, and there is a large diversity. Even in our dataset, several samples contain more than one pith, which will may also negatively affect the performance.

Finally, we employed a two-step technique to determine the tree growth ring alignment with reference points. Future work could explore object detection algorithms with key point identification to improve the performance and include additional species.

4. Conclusions

We introduced a new dataset of images of hardwood species annotated for tree ring detection (see Table 1). It currently consists of 136 cookies of 11 common hardwood species from Indiana, USA. We obtained images of both rough, chain-saw cut surfaces, as well as smooth, cleanly machined, and sanded surfaces. By applying the state-of-the-art deep learning method to detect growth ring edges in clean images, we achieved an overall pixel-level score $AUC = 85.72\%$ and ring level score $F_1 = 0.7348$.

CRediT authorship contribution statement

Fanyou Wu: Conceived the research idea, Collected and annotated the dataset, Wrote the manuscript. **Yunmei Huang:** Collected and annotated the dataset. **Bedrich Benes:** Conceived the research idea, Reviewed and edited the manuscript. **Charles C. Warner:** Collected and annotated the dataset, Wrote the manuscript. **Rado Gazo:** Conceived the research idea, Reviewed and edited the manuscript.

Declaration of competing interest

The authors declare that they have no known competing financial interests or personal relationships that could have appeared to influence the work reported in this paper.

Data availability

The data and code are available at https://github.com/wufanyou/growth-ring-detection.

References

[1] Douglass AE. Climatic cycles and tree-growth. Vol. 2. Carnegie Institution of Washington; 1919.

[2] Ferguson CW. Bristlecone pine: Science and esthetics: A 7100-year tree-ring chronology aids scientists; Old trees draw visitors to California mountains. Science 1968;159(3817):839–46. http://dx.doi.org/10.1126/science.159.3817.839.

[3] LaMarche VC. Tree-ring evidence of past climatic variability. Nature 1978;276(5686):334–8. http://dx.doi.org/10.1038/276334a0.

[4] Ballesteros J, Bodoque J, Díez-Herrero A, Sanchez-Silva M, Stoffel M. Calibration of floodplain roughness and estimation of flood discharge based on tree-ring evidence and hydraulic modelling. J Hydrol 2011;403(1–2):103–15. http://dx.doi.org/10.1016/j.jhydrol.2011.03.045.

[5] Wiles GC, Calkin PE, Jacoby GC. Tree-ring analysis and quaternary geology: Principles and recent applications. Geomorphology 1996;16(3):259–72. http://dx.doi.org/10.1016/s0169-555x(96)80005-5.

[6] Norell K. Automatic counting of annual rings on pinus sylvestris end faces in Sawmill industry. Comput Electron Agric 2011;75(2):231–7. http://dx.doi.org/10.1016/j.compag.2010.11.005.

[7] Hoadleym RB. Identifying wood: accurate results with simple tools. Taunton Press; 1990.

[8] Shi J, Xiang W, Liu Q, Shah S. MtreeRing: An R package with graphical user interface for automatic measurement of tree ring widths using image processing techniques. Dendrochronologia 2019;58:125644. http://dx.doi.org/10.1016/j.dendro.2015.04.002.

[9] Soille P, Misson L. Tree ring area measurements using morphological image analysis. Can J Forest Res 2001;31(6):1074–83. http://dx.doi.org/10.1139/x01-025.

[10] Cerda M, Hitschfeld-Kahler N, Mery D. Robust tree-ring detection. In: Advances in image and video technology. Springer Berlin Heidelberg; 2007, p. 575–85. http://dx.doi.org/10.1007/978-3-540-77129-6_50.

[11] Fabijańska A, Danek M, Barniak J, Piórkowski A. Towards automatic tree rings detection in images of scanned wood samples. Comput Electron Agric 2017b;140:279–89. http://dx.doi.org/10.1016/j.compag.2017.06.006.

[12] Fabijańska A, Danek M. DeepDendro – a tree rings detector based on a deep convolutional neural network. Comput Electron Agric 2018;150:353–63. http://dx.doi.org/10.1016/j.compag.2018.05.005.

[13] Ronneberger O, Fischer P, Brox T. U-Net: convolutional networks for biomedical image segmentation. Springer International Publishing; 2015, p. 234–41. http://dx.doi.org/10.1007/978-3-319-24574-4_28.

[14] Habite T, Abdeljaber O, Olsson A. Automatic detection of annual rings and pith location along norway spruce timber boards using conditional adversarial networks. Wood Sci Technol 2021;55(2):461–88. http://dx.doi.org/10.1007/s00226-021-01266-w.

[15] Isola P, Zhu J-Y, Zhou T, Efros AA. Image-to-image translation with conditional adversarial networks. In: 2017 IEEE conference on computer vision and pattern recognition. IEEE; 2017, http://dx.doi.org/10.1109/cvpr.2017.632.

[16] Goodfellow IJ, Pouget-Abadie J, Mirza M, Xu B, Warde-Farley D, Ozair S, et al. Generative adversarial nets. In: Proceedings of the 27th international conference on neural information processing systems. Vol. 2. MIT Press; 2014, p. 2672–80. http://dx.doi.org/10.5555/2969033.2969125.

[17] Fabijańska A, Danek M, Barniak J, Piórkowski A. A comparative study of image enhancement methods in tree-ring analysis. In: Image processing and communications challenges. Vol. 8. Springer International Publishing; 2017a, p. 69–78. http://dx.doi.org/10.1007/978-3-319-47274-4_8.

[18] Lin T-Y, Dollar P, Girshick R, He K, Hariharan B, Belongie S. Feature pyramid networks for object detection. In: 2017 IEEE conference on computer vision and pattern recognition. IEEE; 2017, http://dx.doi.org/10.1109/cvpr.2017.106.

[19] He K, Zhang X, Ren S, Sun J. Deep residual learning for image recognition. In: 2016 IEEE conference on computer vision and pattern recognition. IEEE; 2016, http://dx.doi.org/10.1109/cvpr.2016.90.

[20] Sandler M, Howard A, Zhu M, Zhmoginov A, Chen L-C. Mobilenetv2: Inverted residuals and linear bottlenecks. In: Proceedings of the IEEE conference on computer vision and pattern recognition. 2018, p. 4510–20. http://dx.doi.org/10.1109/CVPR.2018.00474.

[21] Tan M, Le Q. EfficientNet: Rethinking model scaling for convolutional neural networks. In: Kamalika C, Ruslan S, editors. Proceedings of the 36th international conference on machine learning. Vol. 97. PMLR; 2019, p. 6105–14, https://proceedings.mlr.press/v97/tan19a.html.

[22] Rahman MA, Wang Y. Optimizing intersection-over-union in deep neural networks for image segmentation. Springer International Publishing; 2016, p. 234–44. http://dx.doi.org/10.1007/978-3-319-50835-1_22.

[23] Duque-Arias D, Velasco-Forero S, Deschaud J-E, Goulette F, Serna A, Decencière E, et al. On power Jaccard losses for semantic segmentation. In: VISAPP 2021: 16th international conference on computer vision theory and applications. 2021.

[24] Kingma DP, Ba J. Adam: A method for stochastic optimization. 2014, arXiv preprint arXiv:1412.6980.

[25] Singh OI, Sinam T, James O, Singh TR. Local contrast and mean thresholding in image binarization. Int J Comput Appl 2012;51(6). http://dx.doi.org/10.5120/8044-1362.

[26] Zhang TY, Suen CY. A fast parallel algorithm for thinning digital patterns. Commun ACM 1984;27(3):236–9. http://dx.doi.org/10.1145/357994.358023.

[27] Gazo R, Vanek J, Abdul-Massih M, Benes B. A fast pith detection for computed tomography scanned hardwood logs. Comput Electron Agric 2020;170:105107. http://dx.doi.org/10.1016/j.compag.2019.105107.